

# Nanowire Architectures Improve Ion Uptake Kinetics in Conjugated Polymer Electrochemical Transistors

Rajiv Giridharagopal, Jiajie Guo, Jessica Kong, and David S. Ginger\*



Cite This: *ACS Appl. Mater. Interfaces* 2021, 13, 34616–34624



Read Online

ACCESS |

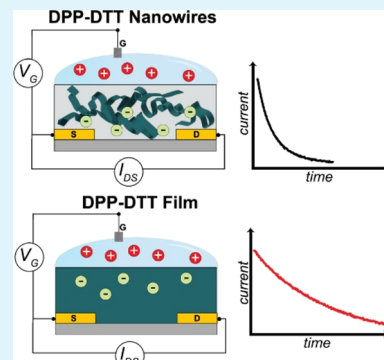
Metrics & More

Article Recommendations

SI Supporting Information

**ABSTRACT:** Organic electrochemical transistors are believed to face an inherent material design tension between optimizing for ion mobility and for electronic mobility. These devices transduce ion uptake into electrical current, thereby requiring high ion mobility for efficient electrochemical doping and rapid turn-on kinetics and high electronic mobility for the maximum transconductance. Here, we explore a facile route to improve operational kinetics and volumetric capacitance in a high-mobility conjugated polymer (*poly*[2,5-(2-octyldodecyl)-3,6-diketopyrrolopyrrole-*alt*-5,5-(2,5-di(thien-2-yl)thieno [3,2-*b*]thiophene)], DPP-DTT) by employing a nanowire morphology. For equivalent thicknesses, the DPP-DTT nanowire films exhibit consistently faster kinetics (~6–10× faster) compared to a neat DPP-DTT film. The nanowire architectures show ~4× higher volumetric capacitance, increasing from 7.1 to 27.7 F/cm<sup>3</sup>, consistent with the porous structure better enabling ion uptake throughout the film. The nanowires also exhibit a small but energetically favorable shift in a threshold voltage of ~17 mV, making the nanostructured system both faster and energetically easier to electrochemically dope compared to neat films. We explain the variation using two atomic force microscopy methods: *in situ* electrochemical strain microscopy and nanoinfrared imaging via photoinduced force microscopy. These data show that the nanowire film's structure allows greater swelling and ion uptake throughout the active layer, indicating that the nanowire architecture exhibits volumetric operation, whereas the neat film is largely operating via the field effect. We propose that for higher-mobility materials, casting the active layer in a nanowire form may offer faster kinetics, enhanced volumetric capacitance, and possibly lower threshold voltage while maintaining desirable device performance.

**KEYWORDS:** organic electrochemical transistors, volumetric capacitance, photoinduced force microscopy, electrochemical strain microscopy, nanowires, DPP-DTT



## INTRODUCTION

Conjugated polymers have seen increasing use in mixed electronic–ionic devices in recent years,<sup>1,2</sup> from polymeric supercapacitors<sup>3,4</sup> to neuromorphic computing architectures<sup>5–7</sup> and organic electrochemical transistors (OECTs) for biosensing.<sup>8–14</sup> The push for better devices has spurred rapid advances in understanding the basic material properties in these organic mixed ionic–electronic conductors that influence OECT operation. OECTs operate by transducing ion uptake into electrical conductivity, where the source of ions is typically an aqueous electrolyte serving as the gate dielectric. The application of a gate bias ( $V_G$ ) to the electrolyte induces ion motion into (or out of)<sup>15</sup> the semiconductor to compensate for an injected electronic charge, resulting in electrochemical doping of the active layer and an increase in the source-drain current,  $I_{DS}$ . Understanding the mechanisms underlying this ion uptake process is critical for enabling rational design of OECT materials.<sup>16</sup> For example, polymeric semiconductors exhibit variations in ion uptake due to crystallinity,<sup>17,18</sup> anion species,<sup>14,19</sup> side-chain functionalization,<sup>18,20–22</sup> and water uptake from aqueous electrolytes.<sup>14,23,24</sup>

OECTs offer the benefit of volumetric capacitance, wherein the three-dimensional active layer accommodates ions and therefore dramatically increases the capacitance,<sup>25</sup> as opposed to purely field-effect operation near the electrolyte–semiconductor interface as in electrolyte-gated field-effect transistors (FETs). The commonly used metric of performance when evaluating an OECT is the product of carrier mobility ( $\mu$ ) and the volumetric capacitance ( $C^*$ ),<sup>26</sup>  $\mu C^*$ . The transconductance ( $dI_{DS}/dV_G$ , or  $g_m$ ) and  $\mu C^*$  are linked through the conventional field-effect transistor equation, which, in the saturation regime, is given by

$$\frac{\Delta I_{DS}}{\Delta V_G} = g_m = \mu C^* \frac{Wd}{L} (V_T - V_G) \quad (1)$$

Received: May 3, 2021

Accepted: July 5, 2021

Published: July 16, 2021



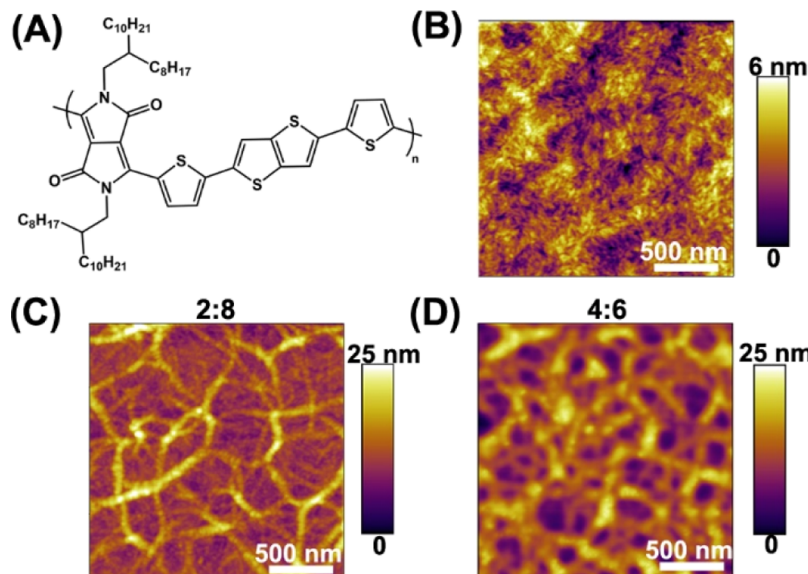


**Figure 1.** DPP-DTT films of different nanowire geometries. (A) Chemical structure of DPP-DTT and (B) DPP-DTT neat films (not nanowires), ~45–50 nm thick. (C) DPP-DTT nanowires formed using a 2:8 DPP-DTT:PS solution and then removing the PS using toluene, ~35–40 nm thick. (D) Nanowires using a 4:6 ratio, ~40–45 nm thick.

Here,  $I_{DS}$  is the source-drain current,  $\mu$  is the carrier mobility ( $\text{cm}^2 \text{V}^{-1} \text{s}^{-1}$ ),  $C^*$  is the volumetric capacitance ( $\text{F}/\text{cm}^3$ ),  $W$  is the channel width,  $L$  is the channel length between the source and drain electrodes,  $d$  is the film thickness,  $V_T$  is the threshold voltage, and  $V_G$  is the gate voltage. From this equation, the key material-related factor in enabling high  $g_m$  is  $\mu C^*$ , where  $\mu$  largely depends on the order in the polymer and  $C^*$  depends upon the ability to store charge throughout the film via ion injection. Although not captured directly by the  $\mu C^*$  product, we emphasize here that turn-on kinetics are also an important design consideration. Although a large  $C^*$  is desirable, if the turn-on/turn-off kinetics are too slow, the material will remain impractical for many applications, such as subsecond recording of electrophysiological activity.<sup>27</sup> Thus, an ideal OEET material architecture would allow efficient ion injection throughout the film (high  $C^*$ , rapidly achieved) while conducting electronic charge through a highly ordered subset of active sites (high  $\mu$ ).<sup>28</sup> In organic FETs (OFETs), many groups have reported that polymer nanowires can enable enhanced mobility,<sup>28–31</sup> and for electrochemical applications, these structures could enable efficient volumetric doping due to the geometrical advantages of high-surface-area nanowire geometries. Indeed, many approaches to improve OEET performance, from acid treatment<sup>32,33</sup> and ionic liquid-based enhancement<sup>34</sup> of PEDOT:PSS to freeze-drying/lyophilization,<sup>35,36</sup> may already result in nanotexturing of the conjugated polymer semiconductor. Herein, we explicitly consider nanowire architectures.

For high- $\mu$  materials, diketopyrrolopyrrole polymers have been reported in a few electrochemical devices.<sup>37,38</sup> As field-effect transistor materials, these semiconducting polymers exhibit some of the highest reported hole mobilities, on the order of  $10 \text{ cm}^2 \text{ V}^{-1} \text{ s}^{-1}$ ,<sup>39–41</sup> thereby enabling high  $g_m$  values while also offering potential advantages in ambipolar transport for more complex device topologies.<sup>41</sup> Recent reports have shown that the donor–acceptor polymer poly[2,5-(2-octyldodecyl)-3,6-diketopyrrolopyrrole-*alt*-5,5-(2,5-di(thien-2-yl)-thieno [3,2-*b*]thiophene)] (DPP-DTT) (Figure 1A) can be made into nanowire structures by mixing with polystyrene

(PS) in a common solvent and exploiting the different relative solubility of the components to remove the PS,<sup>42</sup> similar to work performed in other DPP-based polymers<sup>43</sup> and more broadly in the OFET community.<sup>31</sup>

Given the advantages of high hole mobility, straightforward nanowire formation, and existing interest in DPP-based polymers for aqueous electrolyte devices, DPP-DTT is a natural platform to test the hypothesis that nanowire morphologies could improve OEET operation. Here, we report the use of DPP-DTT in OEETs and demonstrate that nanowires consistently enable 6–10× faster ion uptake compared to the standard (neat) DPP-DTT film, while maintaining similar  $\mu C^*$ . We show consistently lower threshold voltages for nanowire films and that nanowires enable higher  $C^*$  values. Finally, we use electrochemical strain microscopy (ESM) and photoinduced force microscopy (PiFM) to verify that the nanowires are accommodating ions directly throughout the bulk of the film rather than merely enabling more efficient field-effect functionality or simply exhibiting higher mobility, thereby showing that nanowires enable enhanced volumetric capacitance compared to the field-effect operation of unstructured DPP-DTT.<sup>39</sup> We find that the device benefit is primarily from the volumetric capacitance. While the hydrophobic nature and highest occupied molecular orbital (HOMO) level of  $-5.2 \text{ eV}$ <sup>40</sup> preclude DPP-DTT specifically from becoming a champion OEET material, this method of enabling faster kinetics with the same device performance is a useful platform for maximizing OEET functionality in a given system, for example, in emerging glycolated DPP derivatives.<sup>14,44–46</sup> Such a method is useful in the context of enabling rational design of faster or more sensitive OEET-based biosensors.<sup>47</sup>

## RESULTS AND DISCUSSION

We formed DPP-DTT nanowires by blending DPP-DTT and PS in a common solvent with varying ratios. The different solubilities result in segregation and ultimately the formation of DPP-DTT nanowires in solution.<sup>40</sup> Hereafter, we refer to these samples in terms of DPP-DTT:PS ratio in solution. A 2:8 ratio

means 1 mL of 20 mg/mL DPP-DTT was added to 4 mL of 20 mg/mL PS (see the Experimental Section). A 1:0 ratio means a neat DPP-DTT solution (no PS). For the blended films, the PS is then removed from the cast films by submerging them in toluene for  $\sim 3\text{--}5$  min; this process can be verified by imaging the same area before and after washing using atomic force microscopy (AFM) (Figure S1) and by spectroelectrochemistry (Figure S11). For the films mentioned here, unless mentioned otherwise, the concentration of DPP-DTT in the combined solution was kept at 4 mg/mL, and we use the terms “nanowire film” and “neat film” to describe a structured nanowire active layer and an unstructured active layer (no PS), respectively. This process yields films of thickness  $\sim 35\text{--}55$  nm based on AFM measurements, with higher values for neat films and lower for 2:8 nanowires, but very different structures (Figure 1B–D). The 2:8 nanowires are easily observed (Figure 1C), while 4:6 are evident but less anisotropic (Figure 1D). The topography for neat films (Figure 1B) is similar to that reported in other works.<sup>42</sup>

**Device Measurements.** We first show that the nanowire films form functional OECTs through conventional device measurements. In these devices, we used a Ag/AgCl electrode as a gate electrode and we used 100 mM potassium hexafluorophosphate ( $\text{KPF}_6$ ) as the electrolyte. For these devices,  $V_T$  is typically around  $-0.5$  V in  $\text{KPF}_6$ ; using  $\text{Cl}^-$  as the anion pushes the  $V_T$  to nearly  $-0.75$  V as seen in other reports,<sup>44</sup> resulting in many cases where the  $g_m$  value does not reach a peak within the electrochemical water window. Given that the focus on our study is the nanowire geometry and not the anion dependence, we use 100 mM  $\text{KPF}_6$  to ensure that  $g_m$  values reach a peak that can be compared across geometries.

Figure 2A shows typical transfer and  $g_m$  curves for our DPP-DTT OECT devices, with representative output curves in Figure S2. Here, the threshold voltage is slightly more negative ( $\sim 17$  mV) for 1:0 than for 4:6 and 2:8 films, indicating that it is energetically easier for anions to dope the nanowire films and enable conduction regardless of W/L (Figure S3). In Figure S2, we show the normalized  $g_m$  value average over many devices ( $\sim 35\text{--}40$  devices tested per ratio). This threshold shift occurs at very slow sweep rates (20 s per 0.025 V step, see the Experimental Section), with no observable hysteresis between forward and reverse sweeps at these rates, indicating that it is a physical effect and not from experimental artifact. This effect is similar to the  $V_T$  shift observed in DPP-DTT nanowire OFETs.<sup>47</sup>

We show aggregated device data for the three different dimensions in Figure 2B and Table 1. These data are aggregated by varying the electrode geometry (see the Experimental Section), and error bars represent the standard deviation of the mean for devices of the same W/L dimensions. The devices exhibit similar  $g_m$ , and using eq 1, we can extract an approximate  $\mu C^*$  from these data. The  $\mu C^*$  data indicate that these all operate with a similar performance on the order of  $\sim 100$  F/cm $\cdot$ V $\cdot$ s. Notably, these devices are similar despite the 1:0 neat film being  $\sim 10$  nm ( $\sim 15\%$ ) thicker on average than 2:8 nanowire device films. As  $g_m$  is well-known to scale with the active layer thickness due to volumetric capacitance,<sup>48</sup> if the active layer thickness was the sole cause of the differences between these films, then the 2:8 nanowires would perform significantly worse than the neat films. Variations in the largest devices ( $W/L = 200$ ) are attributed to increases in contact resistance (or other parasitic resistance) from ion concentration at the drain due to larger geometry.<sup>49</sup>

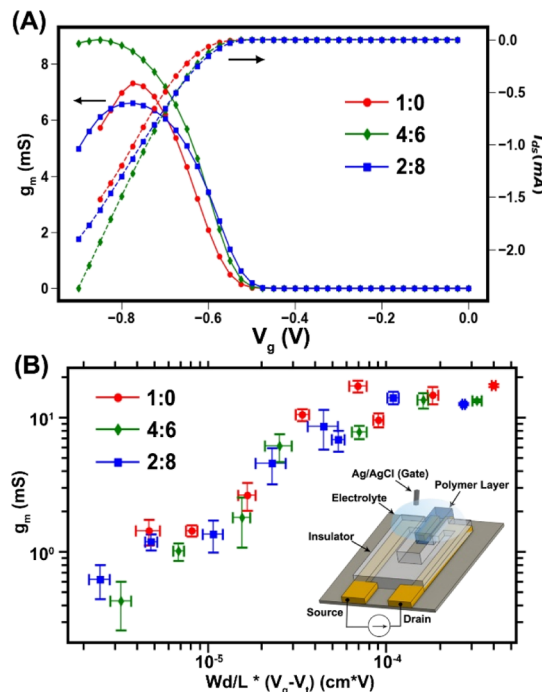


**Figure 2.** DPP-DTT OECT device data. (A) Typical transfer curve and transconductance for 1:0, 4:6, and 2:8 films in 100 mM  $\text{KPF}_6$ , plotted vs gate-source voltage  $V_G$ . (B)  $g_m$  statistics plotted against the DPP-DTT structure. Here, the data are averaged for devices of the same  $W/L$  ratio with the film thickness held approximately constant, and error bars represent standard deviation of the mean  $g_m$  value and the  $(V_G - V_T)$  value, where  $V_G$  is the gate voltage for peak  $g_m$ . Inset: device schematic for the OECT devices used here.

By comparing the data to electrochemical impedance spectroscopy (EIS), we observe an improvement in the volumetric capacitance ( $C^*$ ). The 1:0, 4:6, and 2:8 films show volumetric capacitance values of  $\sim 7.1$ ,  $8.7$ , and  $27.7$  F/cm $^3$ , respectively (Figures S12 and S13). By measuring the mobility via saturation current, we extract hole mobilities on the order of  $\sim 7$  cm $^2$  V $^{-1}$  s $^{-1}$ , with the 2:8 nanowires having similar if slightly lower mobility than 1:0 neat films if calculating via  $\mu C^*$  and EIS ( $5.6$  cm $^2$  V $^{-1}$  s $^{-1}$  compared to  $16$  cm $^2$  V $^{-1}$  s $^{-1}$ , Table 1). While at first surprising, the complex structure–function relationship in aqueous gating has a significant effect on the electronic behavior. For example, it has been shown that increasing the dry mobility can decrease the OECT mobility due to the effect of hydration on the polymer structure.<sup>49</sup> We discuss the competing effects of swelling and crystalline structure on kinetics, mobility, and volumetric capacitance below.

The nanowire architecture favorably shifts the threshold voltage while maintaining similar current-transport properties to a conventional film. This threshold voltage shift could occur because the nanowires shift the HOMO level to enable easier oxidation, as is common with more ordered conjugated polymer films,<sup>50</sup> or the nanowires could enable better accessibility to the three-dimensional volume of the film. While  $g_m$  scales with film thickness,<sup>48</sup> device data are acquired under steady-state conditions and cannot discriminate between these possibilities alone. Device kinetics indicate that the 2:8 nanowire case exhibits faster  $I_{DS}$  (18% up to 47%) in response to a gate voltage step (from 0 to  $-0.8$  V) compared to the neat film (Figure S4) with reasonably similar cycling stability

Table 1. OECT Characteristics of DPP-DTT Devices<sup>a</sup>

DPP-DTT ratio	$V_T$ (V)	$g_m/(Wd/L)$ (S cm <sup>-1</sup> )	$\mu C^*$ (F cm <sup>-1</sup> V <sup>-1</sup> s <sup>-1</sup> )	$C^*$ (F cm <sup>-3</sup> )	$\mu_{OECT}$ (cm <sup>2</sup> V <sup>-1</sup> s <sup>-1</sup> ) (saturation)	$\mu$ (cm <sup>2</sup> V <sup>-1</sup> s <sup>-1</sup> ) (calculated from $\mu C^*$ )	$I_{on}/I_{off}$
1:0	$-0.519 \pm 0.02$	56.5	123.4	$7.1 \pm 0.6$	$7.28 \pm 1.3$	17.3	$\sim 10^5$
4:6	$-0.509 \pm 0.03$	68.0	107.2	$8.7 \pm 0.9$	$7.38 \pm 1.1$	12.3	$\sim 10^4$
2:8	$-0.502 \pm 0.01$	77.5	132.3	$27.7 \pm 1.1$	$7.16 \pm 1.0$	4.8	$\sim 10^5$

<sup>a</sup>  $g_m$  is averaged across device channels for the data in Figure 2B and normalized by  $Wd/L$  to account for device geometry.  $C^*$  values are extracted from EIS.  $\mu_{OECT}$  is taken from transistor output data operating in saturation.

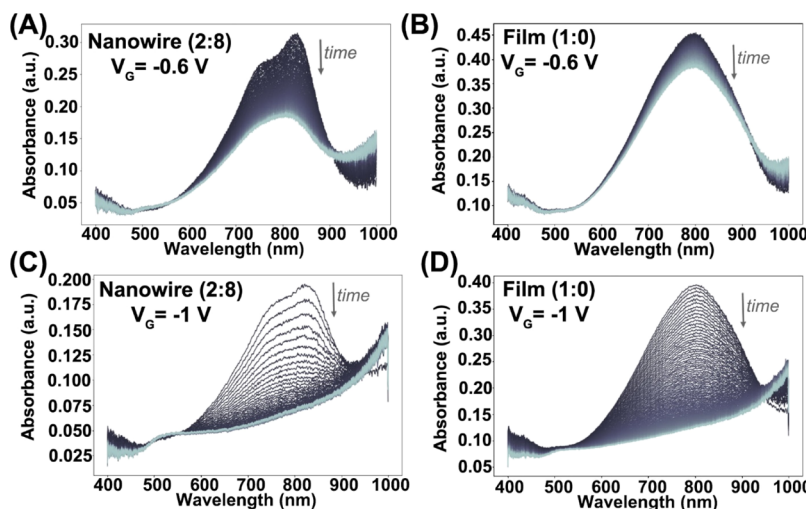


**Figure 3.** Spectroelectrochemistry of DPP-DTT nanowires versus neat films. (A) Absorbance spectra with the gate (Ag/AgCl) at  $-0.6$  V, barely beyond  $V_T$ , for 2:8 nanowires and (B) 1:0 neat film. Spectra are acquired during the first 20 s after a gate bias is applied. (C) Absorbance spectra with the gate at  $-1$  V for 2:8 nanowires and (D) 1:0 neat film.  $-1$  V is far beyond  $V_T$  for these materials. These data show the significant kinetic benefit from nanowires under near threshold voltage conditions and under saturation conditions. These data were taken in 100 mM KPF<sub>6</sub>.

(Figure S5). For the remainder of this work, we focus on the two extreme cases (2:8 and 1:0) to better examine how nanostructuring can improve operation. Although EIS can also be used to extract characteristic time constants,<sup>S1</sup> we primarily use time-dependent measurements for direct comparison.

**Spectroelectrochemistry.** We next use spectroelectrochemistry to investigate the kinetics and the mechanism involved in ion uptake. To better focus on the difference between DPP-DTT nanowire networks and neat films in the context of electrochemical transistors, we turn our attention primarily to comparing 2:8 and 1:0 films. In Figure 3A,B, we compare the spectra taken in KPF<sub>6</sub> at different voltages over 20 s. For the nanowires, we see clear evidence of vibronic peaks associated with the highly crystalline structures,<sup>S2</sup> with a 0–0 vibrational peak at  $\sim 820$  nm red-shifted relative to the peak absorption in the neat film at  $\sim 800$  nm, similar to that reported for DPP-DTT nanowires under dry conditions.<sup>S2</sup> These spectra indicate that the 2:8 film is more highly ordered. Zhang et al. showed that DPP-DTT films are crystalline in the bulk but disordered at the liquid interface;<sup>S3</sup> our results with thicker DPP-DTT films (Figure S6) match this interpretation, with  $\sim 130$  nm films showing these vibronic spectra due to higher percentage of the film being inaccessible to the water layer. We propose that the nanowires seem to retain a higher level of crystallinity at the liquid interface compared to the neat films.

Upon application of a gate voltage just beyond  $V_T$  (Figure 3A,B, where  $V_G = -0.6$  V), the spectra for the nanowires exhibit a clear bleach of the  $\pi-\pi^*$  peak centered  $\sim 800$  nm and an associated increase in polaron absorption  $>900$  nm. For the film, this process over the same period is much slower. At

higher bias far beyond threshold (Figure 3C,D, where  $V_G = -1$  V), the process is faster in both neat films and nanowire films. An initial assumption might be that the kinetics are faster only due to the favorable shift in threshold voltage when using the nanowires. To rule out this effect, we plot the kinetics at 800 nm across a range of bias voltages in Figure 4A. Here, the time constants show a clear difference between the two geometries. Figure 4A plots the time constant based on a single exponential fit to the kinetics for a range of  $V_G > V_T$  (when the device is turned on). At just beyond threshold, the nanowires are  $\sim 6\times$  faster, and at  $-1$  V (saturation), they are  $\sim 10\times$  faster. As suspected from the  $V_T$  shift in the device data, the nanowires are indeed easier to electrochemically dope than the unstructured film. The threshold can be estimated from the absorbance data (Figures S6B and S7) as well as cyclic voltammetry (Figure S14), showing the same threshold voltage shift between nanowires and films. This difference in kinetics holds across wavelengths at each voltage (Figures 4B, S8), indicating that the kinetics variation is more than just threshold voltage shift between the film and nanowire and unrelated to the toluene wash (Figure S9). Here, the plots show the rate ( $1/\tau$ ,  $\tau$  is the single exponential time constant) for the sake of clarity. Switching from KPF<sub>6</sub> to NaCl significantly slows down the kinetics (Figure S10), but the comparative behavior of nanowires versus films remains the same (i.e., nanowire films still show  $\sim 1.5\text{--}2\times$  faster kinetics). While  $\mu C^*$  could be impacted by thickness because of the increased accessibility of polymer or diffusion-limited transport,<sup>S4</sup> the kinetic trends across various thicknesses seem to rule that out as the sole contributing factor (Figure 4C).

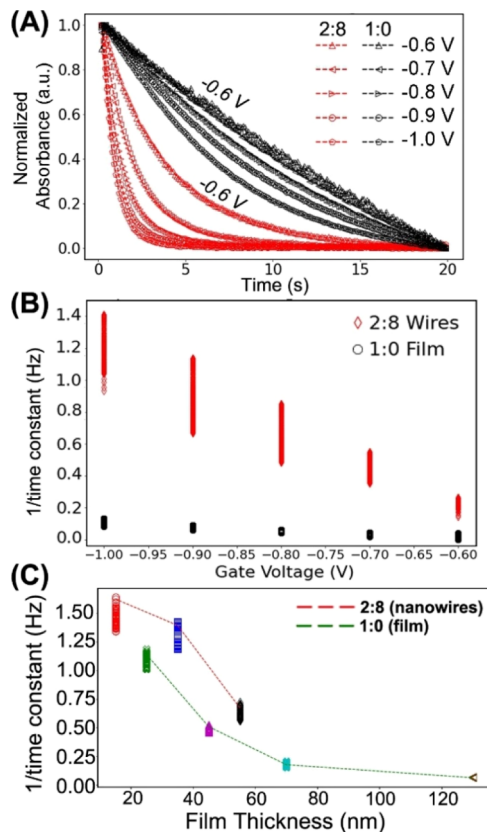


**Figure 4.** Kinetics of DPP-DTT nanowires vs neat films. (A) Normalized absorbance versus time for 2:8 (nanowire) and 1:0 (neat) films from  $-0.6$  to  $-1.0$  V at 800 nm, spanning conditions barely above threshold and far above threshold, respectively. The curve corresponding to  $-0.6$  V for each ratio is labeled for clarity. (B) Rate constant ( $1/\tau$ ,  $\tau$  is the single exponential time constant) as a function of gate voltage. The rate constant shown for each gate voltage is measured from spectroelectrochemistry at each wavelength from 600 to 900 nm. The nanowires are  $\sim 6\text{--}10\times$  faster at each voltage. (C) Rate constant for various thicknesses for 2:8 and 1:0 films, plotted for each rate measured from 730 to 850 nm for each film. These data confirm that the improved kinetics are due to the structure and not just film thickness—at a given overall thickness, the 2:8 devices are faster.

The nanowire geometry therefore seems to permit oxidation of the film both at lower threshold voltage and faster than in the neat film. These data seem to indicate that the nanowires are not necessarily benefiting from enhanced mobility but rather from a morphological effect, wherein the volume of the film is more easily accessible by injected ions. Indeed, studies of poly(3-hexylthiophene) have shown that absorbance kinetics in thin active layers are limited more by ion injection than diffusion within the active layer,<sup>54,55</sup> and we interpret these data as consistent with that observation.

**Scanning Probe Analysis.** Taking these data into account, we turn to scanning probe methods to provide a real-space answer for two remaining questions. First, why does changing the morphology of the film result in an improvement in kinetics? Second, why do the nanowires show higher  $C^*$  but lower  $\mu$ ? To answer these questions, we first probe the nanoscale structure using ESM, which probes the swelling of the polymer *in situ* due to ion injection into the film. In Figure 5, we use ESM as a function of tip-bias for a neat film and a nanowire film. In Figure 5B, we observe swelling all over

the nanowire film (with the topography shown in Figure 5A), and the data show slightly higher swelling in areas between the top-most nanowires. Figure 5C shows a 1:0 film, taken at higher tip bias, showing almost similar amounts of swelling amplitude. Because the AFM cantilever in this case acts as the gate, in Figure 5D, we plot the ESM amplitude as a function of tip voltage for a 2:8 and a 1:0 film. We observe a significant increase in the swelling on the nanowire film beyond threshold voltage conditions (at negative tip voltages) compared to the neat film, which is consistent with enhanced ion injection for the nanowire case.

Finally, we use PiFM on films that have been doped *ex situ* and imaged with  $\text{PF}_6^-$  remaining, as we have done in previous work.<sup>18,56</sup> PiFM is a nanoinfrared AFM method that allows mapping of vibrational spectra with high spatial resolution. The spectra of the nanowires are shown in Figure S15. While the topography in the 2:8 nanowires does not show any obvious structure, the PiFM data reveal the very strong presence of  $\text{PF}_6^-$  ( $\sim 840 \text{ cm}^{-1}$ ) with evidence of the PiFM signal in areas between the topmost wires consistent with uptake into the film (Figures 6, S16). By comparing the data taken on neat films and nanowires at the doping interface, the neat 1:0 films exhibit significant topographic changes at the surface consistent with less ion diffusion into the bulk (Figures S16C and S17). The aggregation of ions near the 1:0 film surface is consistent with previous reports of largely electrolyte-gated field-effect operation as opposed to volumetric operation.<sup>53</sup> These AFM data therefore show that the nanowire benefits relative to the neat film arise primarily from morphology, with the high surface area and nanowire structure better enabling ion uptake. This observation agrees with liquid interfacial studies showing that a disordered  $\sim 2 \text{ nm}$  layer in DPP-DTT can determine charge-transport properties;<sup>53</sup> here, the nanowires are a porous network, and effectively, the volume of the film is perhaps within the liquid interface, given the difference in ESM amplitude.

These scanning probe data also yield a potential hypothesis to address the second question regarding the mobility. As has been shown in previous work,<sup>55</sup> ion uptake and associated water molecules can have surprising effects on the performance by disrupting crystallinity. We hypothesize that because the nanowire films swell more than the neat film during operation, this swelling disrupts the crystallinity of the DPP-DTT nanowire network and decreases the mobility. As a result, despite being able to more easily accommodate ions volumetrically (showing higher  $C^*$ ), the nanowires may also show lower mobility. Future experiments involving, for example, *in situ* grazing incidence wide-angle X-ray scattering<sup>56</sup> may help support this interpretation. Our results thus indicate that nanowire architectures can be a reasonable route to significantly improve volumetric capacitance with a given material, if the associated change in mobility due to swelling can be kept relatively low by optimizing the nanowire structure.

## CONCLUSIONS

We have shown that in a high-mobility polymer, DPP-DTT, we can improve the kinetics by employing nanowire structures instead of a conventional neat film. We demonstrate that while optimizing for mobility is important in OECTs, it is important to consider that  $C^*$  (volumetric capacitance) is linked to how easily ions can diffuse into the three-dimensional volume. The nanowire structures exhibit faster kinetics at all voltages and a

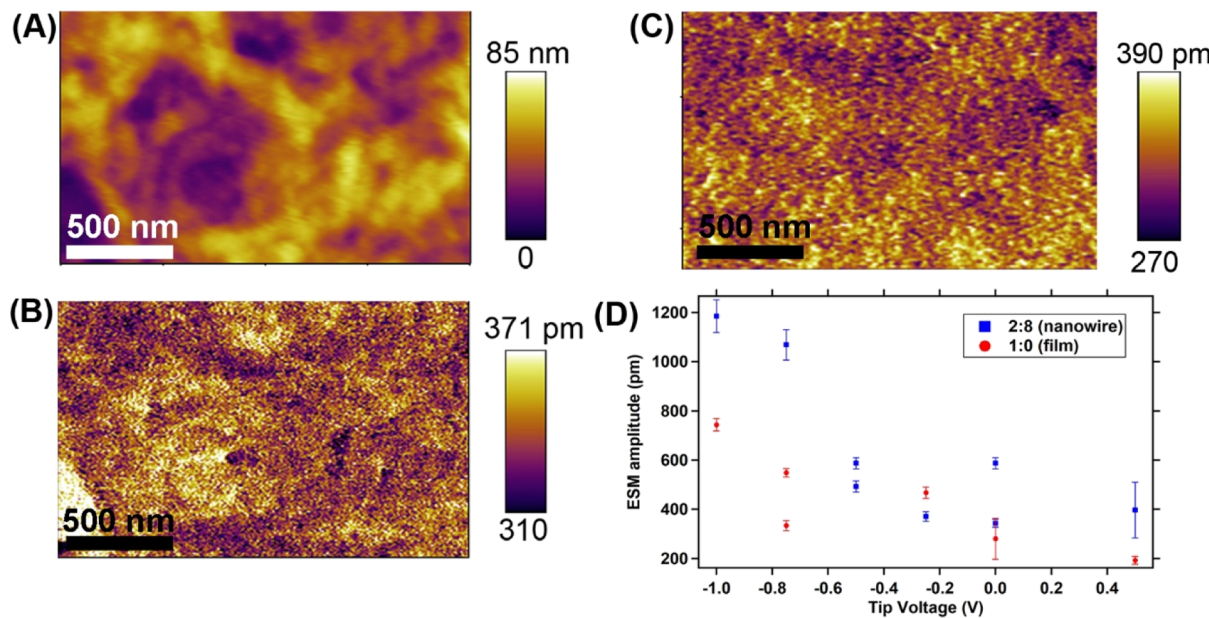


**Figure 5.** ESM amplitude vs geometry. (A) Topography and (B) ESM amplitude of a 2:8 (nanowire) film in 20 mM  $\text{KPF}_6$ . Here, the ESM amplitude is taken with  $V_{\text{AC}} = 500$  mV (i.e., centered at  $0 \text{ V} \pm 250$  mV) and  $V_{\text{tip}} = 0$  V. (C) ESM amplitude for a 1:0 neat film in 20 mM  $\text{KPF}_6$ , with  $V_{\text{tip}} = -0.75$  V. (D) ESM amplitudes for a 2:8 and 1:0 layer across a range of  $V_{\text{tip}}$  values, with the error bars representing standard deviation in the amplitude response. The 2:8 nanowire device shows higher amplitudes than the 1:0 conventional DPP-DTT film, particularly when the  $V_{\text{tip}}$  is past the threshold for consistent doping at  $-0.5$  V. These data are consistent with the hypothesis that the nanowires exhibit enhanced ion uptake due to their geometry relative to the non-nanowire film.

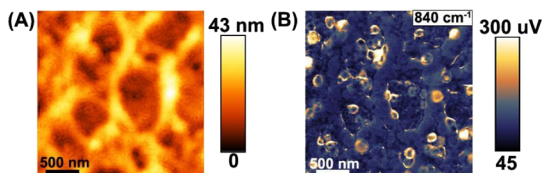


**Figure 6.** PiFM of  $\text{PF}_6^-$  dopants in DPP-DTT nanowires. (A) Topography and (B) PiFM at  $840 \text{ cm}^{-1}$  of a 2:8 DPP-DTT nanowire film, corresponding to the  $\text{PF}_6^-$ . The film was electrochemically doped using 100 mM  $\text{KPF}_6$  and a Ag/AgCl gate at  $V_G = -0.85$  V for  $\sim 60$  s.

slightly lower threshold voltage, which we attribute to the nanowires allowing lower structural barrier for ion diffusion into the film. The nanowires also exhibit higher  $C^*$ . We verify this result through real-space imaging in various correlated AFM modalities, showing that the nanowires indeed swell under bias and that the DPP-DTT system exhibits volumetric response as an OECT rather than through a field effect. Although the hydrophobic nature and comparatively large threshold voltage preclude DPP-DTT from practical OECT device applications, and the limited operational window due to the HOMO level narrows the potential biologically relevant application range, the data here present a platform for simple optimization on the state-of-the-art materials that are under development.

## EXPERIMENTAL SECTION

**Film Formation.** Poly[2,5-(2-octyldodecyl)-3,6-diketopyrrolypyrrole-*alt*-5,5-(2,5-di(thien-2-yl)thieno[3,2-*b*]thiophene)] (DPP-DTT, Ossila) and PS (Sigma-Aldrich) were dissolved separately in dichlorobenzene in a nitrogen glovebox. These solutions were stirred at no higher than  $60$  °C and 600 rpm for at least 2 h. For the ratios specified in the paper (2:8 and 4:6), the solutions were mixed based on the volume ratio. The desired target was 4 mg/mL DPP-DTT per

mL of mixed solution. To achieve this, for 2:8 films, we make separate solutions of DPP-DTT and PS at 20 mg/mL, and for 4:6 films, we make separate solutions at 10 mg/mL. For neat DPP-DTT (i.e., a ratio of 1:0 DPP-DTT:PS), we dissolve at 4 mg/mL. All mixed solutions were stirred at  $60$  °C and 600 RPM overnight. We spin-coat the solution on plasma-cleaned substrates using 3 s at 500 rpm, 150 s at 1500 rpm, and then 10 s at 2000 rpm. Typically, the solutions are heated at approximately  $30$  °C prior to spin-coating. The films are annealed at  $200$  °C under flowing nitrogen for 5 min. For removing PS, we submerge the films in toluene for at least 5 min. The films are then stored in vacuum.

**Device Measurements.** For device measurements, we use custom-fabricated gold electrodes on polyethylene terephthalate substrates (Nano Terra) or evaporated on glass. The electrodes are all with  $20 \mu\text{m}$  channel lengths and channel widths of 4000, 2000, 1000, 800, 400, 200, and  $100 \mu\text{m}$ . Devices are prepared in a similar manner to films using the procedure mentioned above, although for most devices, we anneal at  $180$  °C to avoid warping the polyethylene terephthalate substrate; annealing at either  $180$  or  $200$  °C had no discernible effect on device performance. Prior to measuring the device performance, we remove excess polymer under a microscope using acetone to wet an absorbent swab similar to that in our previous work;<sup>13,18</sup> then, we cover all of the device except the active area and the contact electrodes to the source/drain with clear nail polish (Sally Hansen Insta-Dri Top Coat). Optical images and device data show no damage to the active layer; an example of the substrate is shown in Figure S18. The electrolyte used was typically 100 mM  $\text{KPF}_6$  or 100 mM KCl, with both degassed with nitrogen for  $\sim 10$  min prior to use. The gate electrode is a standard Ag/AgCl electrode. The device measurements are acquired using LabView code that operates two Keithley 2400 source-measure units. This code, along with a Python version, is publicly available upon request. All devices are cycled once prior to measurement, and all the device data shown use both the trace and retrace. Typical measurement times are 20 s per point in the transfer curves (or 800 s/V), with 120 s wait time prior to the first data point to ensure steady-state doping conditions are reached. Analysis was performed using custom Python code; this code is publicly available ([https://github.com/GingerLabUW/oect\\_processing](https://github.com/GingerLabUW/oect_processing)). The threshold voltages are calculated using linear fits

to  $I_{DS}^{1/2}$  versus  $V_G$  plots. Transconductance ( $g_m$ ) was calculated using a derivative of the transfer curve directly.

**Spectroelectrochemistry and Electrochemical Impedance Spectroscopy.** For spectroelectrochemistry, we use a MetroOhm PGSTAT204 to operate our device and an Agilent 8453 spectrometer for recording the data. For these measurements, we spin-coat the film on FTO substrates (Sigma-Aldrich). We use a Ag/AgCl as the reference electrode and a Pt mesh as the counter electrode. We cycle each device with a C–V curve three times prior to measurement. The devices are cycled from –0.9 to 0.9 V at 0.2 V/s and analyzed via the MetroOhm NOVA software. The data are analyzed in Python via the abovementioned publicly available code. For electrochemical impedance, we use  $600 \times 600 \mu\text{m}^2$  and  $1 \times 1 \text{ mm}^2$  Au pads for the substrate, with data taken from 0.1 Hz to 100 kHz, using the same electrode configuration as spectroelectrochemistry. The EIS samples are measured with DC biases from 0 to 0.8 V and an AC voltage of 5 mV. We fit the data using a modified Randles circuit.

**Scanning Probe Microscopy.** AFM measurements were performed on two instruments. The ESM experiments were performed on an Asylum Research Cypher-ES system, as were AM-FM/stiffness measurements. The topography, including scratch edge images for film thickness measurements, and other AFM data were acquired on an MFP-3D. For the ESM data, we use 20 mM KPF<sub>6</sub> as the electrolyte during measurement; for other AFM measurements, the samples are in a closed cell under flowing nitrogen. For PiFM, we used a Molecular Vista VistaScan system with a Block Laser quantum cascade laser capable of infrared excitation from 760 to 1850 cm<sup>–1</sup>. For AM-FM, we typically use Budget Sensors ElectriMulti75-G tips (~2 N/m, ~75 kHz). For PiFM, we use Mikro-Masch HQ:NSC15 tips (~30 N/m, ~325 kHz). For ESM, we use Budget Sensors ContGB tips (~0.2 N/m, ~13 kHz); in ESM, the amplitude can be increased using lower stiffness cantilevers, so users are cautioned to avoid comparing data taken with very different tips. We use the second resonance mode for topography and the first mode for imaging. For the doping experiments, we bias the film relative to a AgCl substrate in 100 mM KPF<sub>6</sub> and then quickly rinse with DI water and dry under nitrogen. The films will show a noticeable color change due to doping; for DPP-DTT, the films become visually clear because of the polaron feature stretching past the visible range.

## ASSOCIATED CONTENT

### Supporting Information

The Supporting Information is available free of charge at <https://pubs.acs.org/doi/10.1021/acsami.1c08176>.

Additional topography data pre-/post-PS removal, device data, additional spectroelectrochemistry in KPF<sub>6</sub> and NaCl data, electrochemical impedance spectroscopy, PiFM spectra, and images of DPP-DTT and PS (PDF)

## AUTHOR INFORMATION

### Corresponding Author

**David S. Ginger** — Department of Chemistry, University of Washington, Seattle, Washington 98195, United States;  
[orcid.org/0000-0002-9759-5447](https://orcid.org/0000-0002-9759-5447); Email: [dginger@uw.edu](mailto:dginger@uw.edu)

### Authors

**Rajiv Giridharagopal** — Department of Chemistry, University of Washington, Seattle, Washington 98195, United States;  
[orcid.org/0000-0001-6076-852X](https://orcid.org/0000-0001-6076-852X)

**Jiajie Guo** — Molecular Engineering and Sciences Institute, University of Washington, Seattle, Washington 98195, United States

**Jessica Kong** — Department of Chemistry, University of Washington, Seattle, Washington 98195, United States;  
[orcid.org/0000-0003-3009-6288](https://orcid.org/0000-0003-3009-6288)

Complete contact information is available at:  
<https://pubs.acs.org/10.1021/acsami.1c08176>

### Notes

The authors declare no competing financial interest.

## ACKNOWLEDGMENTS

This paper is based primarily on preliminary work begun under the National Science Foundation grant DMR-1607242 and completed under DMR-2003456. We acknowledge additional support for data science methods development to analyze the PiFM data (J.K.) from NSF EAGER DMR-1842708. J.K. also received student fellowship support from the Clean Energy Institute and National Science Foundation Research Traineeship under award NSF DGE-1633216. We thank Lucas Q. Flagg and Connor G. Bischak for helpful discussions. Part of this work was conducted at the Molecular Analysis Facility, a National Nanotechnology Coordinated Infrastructure site at the University of Washington which is supported in part by the National Science Foundation (grant NNCI-1542101), the University of Washington, the Molecular Engineering & Sciences Institute, the Clean Energy Institute, and the National Institutes of Health.

## REFERENCES

- (1) Paulsen, B. D.; Tybrandt, K.; Stavrinidou, E.; Rivnay, J. Organic Mixed Ionic-Electronic Conductors. *Nat. Mater.* **2020**, *19*, 13–26.
- (2) Ohayon, D.; Inal, S. Organic Bioelectronics: From Functional Materials to Next-Generation Devices and Power Sources. *Adv. Mater.* **2020**, *32*, 2001439.
- (3) Meng, Q.; Cai, K.; Chen, Y.; Chen, L. Research Progress on Conducting Polymer Based Supercapacitor Electrode Materials. *Nano Energy* **2017**, *36*, 268–285.
- (4) Zhao, Z.; Richardson, G. F.; Meng, Q.; Zhu, S.; Kuan, H.-C.; Ma, J. PEDOT-Based Composites as Electrode Materials for Supercapacitors. *Nanotechnology* **2016**, *27*, 042001.
- (5) van de Burgt, Y.; Lubberman, E.; Fuller, E. J.; Keene, S. T.; Faria, G. C.; Agarwal, S.; Marinella, M. J.; Alec Talin, A.; Salleo, A. A Non-Volatile Organic Electrochemical Device as a Low-Voltage Artificial Synapse for Neuromorphic Computing. *Nat. Mater.* **2017**, *16*, 414–418.
- (6) Keene, S. T.; Melianas, A.; Fuller, E. J.; van de Burgt, Y.; Talin, A. A.; Salleo, A. Optimized Pulsed Write Schemes Improve Linearity and Write Speed for Low-Power Organic Neuromorphic Devices. *J. Phys. D: Appl. Phys.* **2018**, *51*, 224002.
- (7) Keene, S. T.; Lubrano, C.; Kazemzadeh, S.; Melianas, A.; Tuchman, Y.; Polino, G.; Scognamiglio, P.; Cinà, L.; Salleo, A.; van de Burgt, Y.; Santoro, F. A Biohybrid Synapse with Neurotransmitter-Mediated Plasticity. *Nat. Mater.* **2020**, *19*, 969.
- (8) Rivnay, J.; Wang, H.; Fennel, L.; Deisseroth, K.; Malliaras, G. G. Next-Generation Probes, Particles, and Proteins for Neural Interfacing. *Sci. Adv.* **2017**, *3*, No. e1601649.
- (9) Fariati, G. C.; Duongt, D. T.; Salleo, A.; Polyzoidis, C. A.; Logothetidis, S.; Rivnay, J.; Owens, R.; Malliaras, G. G. Organic Electrochemical Transistors as Impedance Biosensors. *MRS Commun.* **2014**, *4*, 189–194.
- (10) Rivnay, J.; Owens, R. M.; Malliaras, G. G. The Rise of Organic Bioelectronics. *Chem. Mater.* **2014**, *26*, 679–685.
- (11) Inal, S.; Rivnay, J.; Sui, A.-O.; Malliaras, G. G.; McCulloch, I. Conjugated Polymers in Bioelectronics. *Acc. Chem. Res.* **2018**, *51*, 1368–1376.

- (12) Rivnay, J.; Inal, S.; Salleo, A.; Owens, R. M.; Berggren, M.; Malliaras, G. G. Organic Electrochemical Transistors. *Nat. Rev. Mater.* **2018**, *3*, 17086.
- (13) Bischak, C. G.; Flagg, L. Q.; Ginger, D. S. Ion Exchange Gels Allow Organic Electrochemical Transistor Operation with Hydrophobic Polymers in Aqueous Solution. *Adv. Mater.* **2020**, *32*, 2002610.
- (14) Flagg, L. Q.; Giridharagopal, R.; Guo, J.; Ginger, D. S. Anion-Dependent Doping and Charge Transport in Organic Electrochemical Transistors. *Chem. Mater.* **2018**, *30*, 5380–5389.
- (15) Flagg, L. Q.; Bischak, C. G.; Quezada, R. J.; Onorato, J. W.; Luscombe, C. K.; Ginger, D. S. P-Type Electrochemical Doping Can Occur by Cation Expulsion in a High-Performing Polymer for Organic Electrochemical Transistors. *ACS Mater. Lett.* **2020**, *2*, 254–260.
- (16) Friedlein, J. T.; McLeod, R. R.; Rivnay, J. Device Physics of Organic Electrochemical Transistors. *Org. Electron.* **2018**, *63*, 398–414.
- (17) Giridharagopal, R.; Flagg, L. Q.; Harrison, J. S.; Ziffer, M. E.; Onorato, J.; Luscombe, C. K.; Ginger, D. S. Electrochemical Strain Microscopy Probes Morphology-Induced Variations in Ion Uptake and Performance in Organic Electrochemical Transistors. *Nat. Mater.* **2017**, *16*, 737–742.
- (18) Flagg, L. Q.; Bischak, C. G.; Onorato, J. W.; Rashid, R. B.; Luscombe, C. K.; Ginger, D. S. Polymer Crystallinity Controls Water Uptake in Glycol Side-Chain Polymer Organic Electrochemical Transistors. *J. Am. Chem. Soc.* **2019**, *141*, 4345–4354.
- (19) Cendra, C.; Giovannitti, A.; Savva, A.; Venkatraman, V.; McCulloch, I.; Salleo, A.; Inal, S.; Rivnay, J. Role of the Anion on the Transport and Structure of Organic Mixed Conductors. *Adv. Funct. Mater.* **2018**, *29*, 1807034.
- (20) Giovannitti, A.; Sbircea, D.-T.; Inal, S.; Nielsen, C. B.; Bandiello, E.; Hanifi, D. A.; Sessolo, M.; Malliaras, G. G.; McCulloch, I.; Rivnay, J. Controlling the Mode of Operation of Organic Transistors through Side-Chain Engineering. *Proc. Natl. Acad. Sci. U.S.A.* **2016**, *113*, 12017–12022.
- (21) Giovannitti, A.; Maria, I. P.; Hanifi, D.; Donahue, M. J.; Bryant, D.; Barth, K. J.; Makdah, B. E.; Savva, A.; Moia, D.; Zetek, M.; Barnes, P. R. F.; Reid, O. G.; Inal, S.; Rumbles, G.; Malliaras, G. G.; Nelson, J.; Rivnay, J.; McCulloch, I. The Role of the Side Chain on the Performance of N-Type Conjugated Polymers in Aqueous Electrolytes. *Chem. Mater.* **2018**, *30*, 2945–2953.
- (22) Roncali, J.; Shi, L. H.; Garreau, R.; Garnier, F.; Lemaire, M. Tuning of the Aqueous Electroactivity of Substituted Poly(Thiophene)s by Ether Groups. *Synth. Met.* **1990**, *36*, 267–273.
- (23) Savva, A.; Cendra, C.; Giugni, A.; Torre, B.; Surgailis, J.; Ohayon, D.; Giovannitti, A.; McCulloch, I.; Di Fabrizio, E.; Salleo, A.; Rivnay, J.; Inal, S. Influence of Water on the Performance of Organic Electrochemical Transistors. *Chem. Mater.* **2019**, *31*, 927–937.
- (24) Moser, M.; Hidalgo, T. C.; Surgailis, J.; Gladisch, J.; Ghosh, S.; Sheelamantula, R.; Thiburce, Q.; Giovannitti, A.; Salleo, A.; Gasparini, N.; Wadsworth, A.; Zozoulenko, I.; Berggren, M.; Stavrinidou, E.; Inal, S.; McCulloch, I. Side Chain Redistribution as a Strategy to Boost Organic Electrochemical Transistor Performance and Stability. *Adv. Mater.* **2020**, *32*, 2002748.
- (25) Proctor, C. M.; Rivnay, J.; Malliaras, G. G. Understanding Volumetric Capacitance in Conducting Polymers. *J. Polym. Sci., Part B: Polym. Phys.* **2016**, *54*, 1433–1436.
- (26) Inal, S.; Malliaras, G. G.; Rivnay, J. Benchmarking Organic Mixed Conductors for Transistors. *Nat. Commun.* **2017**, *8*, 1767.
- (27) Khodagholy, D.; Doublet, T.; Quilichini, P.; Gurinkel, M.; Leleux, P.; Ghestem, A.; Ismailova, E.; Hervé, T.; Sanaur, S.; Bernard, C.; Malliaras, G. G. Vivo Recordings of Brain Activity Using Organic Transistors. *Nat. Commun.* **2013**, *4*, 1575.
- (28) Rivnay, J.; Inal, S.; Collins, B. A.; Sessolo, M.; Stavrinidou, E.; Strakosas, X.; Tassone, C.; Delongchamp, D. M.; Malliaras, G. G. Structural Control of Mixed Ionic and Electronic Transport in Conducting Polymers. *Nat. Commun.* **2016**, *7*, 11287.
- (29) Tatum, W. K.; Luscombe, C. K.  $\pi$ -Conjugated Polymer Nanowires: Advances and Perspectives toward Effective Commercial Implementation. *Polym. J.* **2018**, *50*, 659–669.
- (30) Briseno, A. L.; Mannsfeld, S. C. B.; Jenekhe, S. A.; Bao, Z.; Xia, Y. Introducing Organic Nanowire Transistors. *Mater. Today* **2008**, *11*, 38–47.
- (31) Jo, S. B.; Lee, W. H.; Qiu, L.; Cho, K. Polymer Blends with Semiconducting Nanowires for Organic Electronics. *J. Mater. Chem.* **2012**, *22*, 4244–4260.
- (32) Kim, S.-M.; Kim, C.-H.; Kim, Y.; Kim, N.; Lee, W.-J.; Lee, E.-H.; Kim, D.; Park, S.; Lee, K.; Rivnay, J.; Yoon, M.-H. Influence of PEDOT:PSS Crystallinity and Composition on Electrochemical Transistor Performance and Long-Term Stability. *Nat. Commun.* **2018**, *9*, 3858.
- (33) Kim, Y.; Noh, H.; Paulsen, B. D.; Kim, J.; Jo, I. Y.; Ahn, H.; Rivnay, J.; Yoon, M. H. Strain-Engineering Induced Anisotropic Crystallite Orientation and Maximized Carrier Mobility for High-Performance Microfiber-Based Organic Bioelectronic Devices. *Adv. Mater.* **2021**, *33*, 2007550.
- (34) Wu, X.; Surendran, A.; Ko, J.; Filonik, O.; Herzog, E. M.; Müller-Buschbaum, P.; Leong, W. L. Ionic-Liquid Doping Enables High Transconductance, Fast Response Time, and High Ion Sensitivity in Organic Electrochemical Transistors. *Adv. Mater.* **2019**, *31*, 1805544.
- (35) Wan, A. M.-D.; Inal, S.; Williams, T.; Wang, K.; Leleux, P.; Estevez, L.; Giannelis, E. P.; Fischbach, C.; Malliaras, G. G.; Gourdon, D. 3D Conducting Polymer Platforms for Electrical Control of Protein Conformation and Cellular Functions. *J. Mater. Chem. B* **2015**, *3*, 5040–5048.
- (36) Pitsalidis, C.; Ferro, M. P.; Iandolo, D.; Tzounis, L.; Inal, S.; Owens, R. M. Transistor in a Tube: A Route to Three-Dimensional Bioelectronics. *Sci. Adv.* **2018**, *4*, No. eaat4253.
- (37) Zhang, Y.; Li, J.; Li, R.; Sbircea, D.-T.; Giovannitti, A.; Xu, J.; Xu, H.; Zhou, G.; Bian, L.; McCulloch, I.; Zhao, N. Liquid-Solid Dual-Gate Organic Transistors with Tunable Threshold Voltage for Cell Sensing. *ACS Appl. Mater. Interfaces* **2017**, *9*, 38687–38694.
- (38) Du, W.; Ohayon, D.; Combe, C.; Mottier, L.; Maria, I. P.; Ashraf, R. S.; Fiumelli, H.; Inal, S.; McCulloch, I. Improving the Compatibility of Diketopyrrolopyrrole Semiconducting Polymers for Biological Interfacing by Lysine Attachment. *Chem. Mater.* **2018**, *30*, 6164–6172.
- (39) Xu, H.; Jiang, Y.; Li, J.; Ong, B. S.; Shuai, Z.; Xu, J.; Zhao, N. Spectroscopic Study of Electron and Hole Polarons in a High-Mobility Donor–Acceptor Conjugated Copolymer. *J. Phys. Chem. C* **2013**, *117*, 6835–6841.
- (40) Li, J.; Zhao, Y.; Tan, H. S.; Guo, Y.; Di, C.-A.; Yu, G.; Liu, Y.; Lin, M.; Lim, S. H.; Zhou, Y.; Su, H.; Ong, B. S. A Stable Solution-Processed Polymer Semiconductor with Record High-Mobility for Printed Transistors. *Sci. Rep.* **2012**, *2*, 754.
- (41) Nielsen, C. B.; Turbiez, M.; McCulloch, I. Recent Advances in the Development of Semiconducting DPP-Containing Polymers for Transistor Applications. *Adv. Mater.* **2013**, *25*, 1859–1880.
- (42) Lei, Y.; Deng, P.; Li, J.; Lin, M.; Zhu, F.; Ng, T.-W.; Lee, C.-S.; Ong, B. S. Solution-Processed Donor-Acceptor Polymer Nanowire Network Semiconductors For High-Performance Field-Effect Transistors. *Sci. Rep.* **2016**, *6*, 24476.
- (43) Um, H. A.; Lee, D. H.; Heo, D. U.; Yang, D. S.; Shin, J.; Baik, H.; Cho, M. J.; Choi, D. H. High Aspect Ratio Conjugated Polymer Nanowires for High Performance Field-Effect Transistors and Phototransistors. *ACS Nano* **2015**, *9*, 5264–5274.
- (44) Yang, S.-F.; Liu, Z.-T.; Cai, Z.-X.; Dyson, M. J.; Stingelin, N.; Chen, W.; Ju, H.-J.; Zhang, G.-X.; Zhang, D.-Q. Diketopyrrolopyrrole-Based Conjugated Polymer Entailing Triethylene Glycols as Side Chains with High Thin-Film Charge Mobility without Post-Treatments. *Adv. Sci.* **2017**, *4*, 1700048.
- (45) Moser, M.; Savva, A.; Thorley, K.; Paulsen, B. D.; Hidalgo, T. C.; Ohayon, D.; Chen, H.; Giovannitti, A.; Marks, A.; Gasparini, N.; Wadsworth, A.; Rivnay, J.; Inal, S.; McCulloch, I. Polaron Delocalization in Donor–Acceptor Polymers and Its Impact on

Organic Electrochemical Transistor Performance. *Angew. Chem., Int. Ed.* **2021**, *133*, 7856–7864.

(46) Krauss, G.; Meichsner, F.; Hochgesang, A.; Mohanraj, J.; Salehi, S.; Schmode, P.; Thelakkat, M. Polydiketopyrrolopyrroles Carrying Ethylene Glycol Substituents as Efficient Mixed Ion-electron Conductors for Biocompatible Organic Electrochemical Transistors. *Adv. Funct. Mater.* **2021**, *31*, 2010048.

(47) Pappa, A.-M.; Parlak, O.; Scheiblin, G.; Mailley, P.; Salleo, A.; Owens, R. M. Organic Electronics for Point-of-Care Metabolite Monitoring. *Trends Biotechnol.* **2018**, *36*, 45–59.

(48) Rivnay, J.; Leleux, P.; Ferro, M.; Sessolo, M.; Williamson, A.; Koutsouras, D. A.; Khodagholy, D.; Ramuz, M.; Strakosas, X.; Owens, R. M.; Benar, C.; Badier, J.-M.; Bernard, C.; Malliaras, G. G. High-Performance Transistors for Bioelectronics through Tuning of Channel Thickness. *Sci. Adv.* **2015**, *1*, No. e1400251.

(49) Kaphle, V.; Paudel, P. R.; Dahal, D.; Radha Krishnan, R. K.; Lüssem, B. Finding the Equilibrium of Organic Electrochemical Transistors. *Nat. Commun.* **2020**, *11*, 2515.

(50) Urquhart, S. G.; Martinson, M.; Eger, S.; Murcia, V.; Ade, H.; Collins, B. A. Connecting Molecular Conformation to Aggregation in P3HT Using Near Edge X-Ray Absorption Fine Structure Spectroscopy. *J. Phys. Chem. C* **2017**, *121*, 21720–21728.

(51) Carli, S.; Di Lauro, M.; Bianchi, M.; Murgia, M.; De Salvo, A.; Prato, M.; Fadiga, L.; Biscarini, F. Water-Based PEDOT:Nafion Dispersion for Organic Bioelectronics. *ACS Appl. Mater. Interfaces* **2020**, *12*, 29807–29817.

(52) Brown, P. J.; Thomas, D. S.; Köhler, A.; Wilson, J. S.; Kim, J.-S.; Ramsdale, C. M.; Sirringhaus, H.; Friend, R. H. Effect of Interchain Interactions on the Absorption and Emission of Poly(3-Hexylthiophene). *Phys. Rev. B: Condens. Matter Mater. Phys.* **2003**, *67*, 064203.

(53) Zhang, Y.; Han, G.; Qin, M.; Shen, Y.; Lu, X.; Yi, Y.; Zhao, N. Spectroscopic Study of Charge Transport at Organic Solid–Water Interface. *Chem. Mater.* **2018**, *30*, 5422–5428.

(54) Shiri, P.; Dacanay, E. J. S.; Hagen, B.; Kaake, L. G. Dynamic Charging Mechanism of Organic Electrochemical Devices Revealed with In Situ Infrared Spectroscopy. *J. Phys. Chem. C* **2019**, *123*, 19395–19401.

(55) Shiri, P.; Dacanay, E. J. S.; Hagen, B.; Kaake, L. G. Vogel–Tammann–Fulcher Model for Charging Dynamics in an Organic Electrochemical Transistor. *J. Mater. Chem.* **2019**, *7*, 12935–12941.

(56) Bischak, C. G.; Flagg, L. Q.; Yan, K.; Rehman, T.; Davies, D. W.; Quezada, R. J.; Onorato, J. W.; Luscombe, C. K.; Diao, Y.; Li, C.-Z.; Ginger, D. S. A Reversible Structural Phase Transition by Electrochemically-Driven Ion Injection into a Conjugated Polymer. *J. Am. Chem. Soc.* **2020**, *142*, 7434–7442.